

## Above-threshold ionization processes in xenon and krypton

T. J. McIlrath,\* P. H. Bucksbaum, R. R. Freeman, and M. Bashkansky†  
*AT&T Bell Laboratories, Murray Hill, New Jersey 07974*

(Received 15 December 1986)

A detailed study of above-threshold ionization processes in xenon and krypton is reported. Using well-characterized pulses of 1.06- and 0.532- $\mu\text{m}$  radiation under carefully controlled experimental conditions, measurements of the energy and direction of photoelectrons from Xe and Kr as a function of laser power and polarization were made. Conclusions about the role of ponderomotive potentials in the determination of much of the phenomenology are presented.

### I. INTRODUCTION

In threshold photoionization, the photoelectron kinetic energy is always less than or equal to the incident photon energy  $h\nu$ . Above-threshold ionization (ATI) is the production of higher-energy electrons that have absorbed more photons than the minimum required to overcome the binding energy.<sup>1</sup> Photoionization studies at low light intensities observe only threshold processes, but many high-order nonresonant multiphoton ionization (MPI) experiments are dominated by ATI, particularly for high laser intensities (typically  $10^{10}$  W/cm<sup>2</sup> or more). For example, Fig. 1 shows the photoelectron spectrum of Xe ionized with 1064-nm radiation ( $h\nu=1.16$  eV). The photoelectron-energy peaks are separated by the photon energy and they extend more than 10 eV above the threshold.

ATI experimental spectra display several unexpected features that have attracted much attention. The appearance of so many electron peaks, each presumably representing different numbers of absorbed photons, challenges perturbation theory. Indeed, the high electric fields of a focused pulsed laser (electric fields up to  $10^8$  V/cm) approach atomic binding fields, suggesting that new calculational techniques may be required. In addition, the relative suppression of threshold MPI, the widths of the peaks, and their dependence on polarization and laser intensity have generated much theoretical and experimental interest.

In this paper we will review a series of ATI experiments

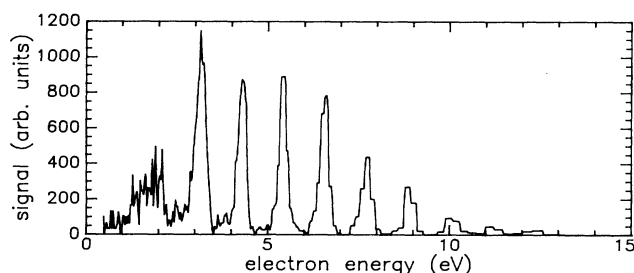


FIG. 1. Electron spectrum from MPI in xenon with 1064-nm light. Laser parameters are  $I_{\text{peak}}=2 \times 10^{13}$  W/cm<sup>2</sup>; energy 11 mJ; duration (full width at half maximum) 100 psec; linear polarization along the detection axis. Detection geometry is shown in Fig. 2.

which we have conducted in Xe and Kr. Our main conclusions, based on analysis of our own results and comparison with other experiments, are as follows.

(1) Scattering of electrons by laser light (so-called “ponderomotive scattering”) plays an important role in the observed photoelectron spectra and angular distributions. In particular, for high intensities the angular distributions are independent of the photoionization processes and are determined by the light-intensity pattern due to final-state scattering of free electrons from the ponderomotive potential of the laser focus as the electrons exit the laser beam.

(2) The atomic ionization potential is shifted by ponderomotive effects so that threshold MPI is forbidden in sufficiently intense fields. Although the inherent spatial inhomogeneity of a focused laser beam makes this effect difficult to observe, we will show how it affects electron yields and angular distributions.

(3) Laser polarization can drastically alter the ATI energy spectra and the photoionization rate. For circular polarization, production of low-energy electrons is greatly suppressed.

(4) Finally, the highly nonlinear nature of MPI requires that careful attention be paid to the effect of the spatial and temporal intensity distributions, and to space charge. We will highlight the significance of these factors and show how a proper integration of their effects can explain several characteristic features of ATI experiments.

Section II is devoted to a description of the experimental apparatus used in all of the subsequent observations. Section III is a summary of the data. The rest of the paper is a detailed analysis of the experiments. In these last sections we describe a model incorporating the electron-light or ponderomotive scattering which provides good quantitative agreement with the experimental results, including the intensity dependence of the angular distributions. We conclude with a summary of those areas of the ATI problem which we feel are now understood, and those which require further investigation.

### II. APPARATUS

#### A. General experimental considerations

Above-threshold ionization is observed by focusing the output of an intense, pulsed laser into an interaction region containing very-low-density gas. The resulting pho-

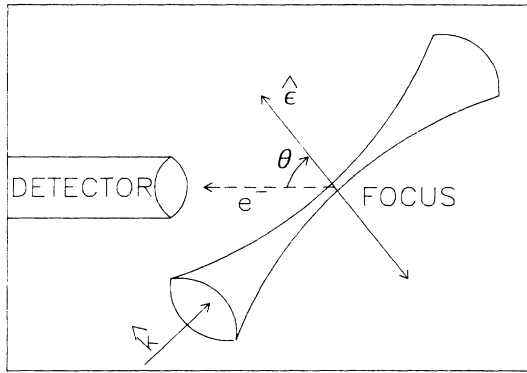


FIG. 2. Detection geometry.

toelectrons are collected and energy analyzed. The geometry is shown in Fig. 2. Although ATI has been observed for laser wavelengths as short as 193 nm,<sup>2</sup> the most dramatic ATI effects are observed with long-wavelength lasers, and our results were all obtained using 1064-nm Nd:YAG laser radiation (1.165 eV; YAG represents yttrium aluminum garnet) or its second harmonic (2.33 eV). The general requirements for the experiment are a clean vacuum to avoid background ionization, a good electron spectrometer in the 0.1–20-eV range, and an intense and well-characterized laser pulse. The experimental apparatus used for our studies is summarized in Fig. 3.

### B. Laser

The important figure of merit for laser strength in ATI experiments is power density  $I$ . Therefore, it is necessary to know accurately the time behavior of the pulse for quantitative studies. We employed a cw Nd:YAG laser (Quantronix 416) that was continuously mode locked to maintain nearly Fourier-transform-limited 100-psec pulses. Its performance was monitored with a scanning Fabry-Perot interferometer. We also performed pulse autocorrelations from time to time, and never observed a coherence spike which might indicate temporal noise. The cavity loss was further modified by an active  $Q$  switch, which dumped the cavity gain at a rate of 10 Hz. A single pulse from the  $Q$ -switched train was selected by a Pockels cell and amplified to 50 mJ in two Nd:YAG amplifiers. If 532-nm light was desired, a KD\*P crystal

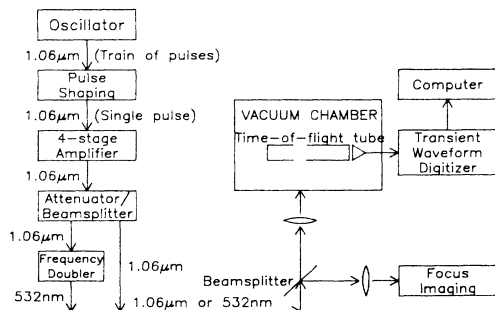


FIG. 3. Block diagram of apparatus, described in text.

was inserted in the amplified beam line, which could produce up to 20 mJ of second-harmonic radiation via angle-tuned type-II frequency doubling.

The spatial profile of the focused laser is equally important for determining the intensity over the interaction volume. The existence of the strong ponderomotive interaction between the radiation field and the electrons makes the profile of the focused beam even more critical in photoelectron angular distribution measurements. The spatial mode in these experiments was formed by an aperture placed directly after the laser oscillator. The resulting Airy pattern was clipped in the far field at the first minimum with a second aperture, and the central maximum was allowed to freely propagate through the amplifier chain and the rest of the optical system.

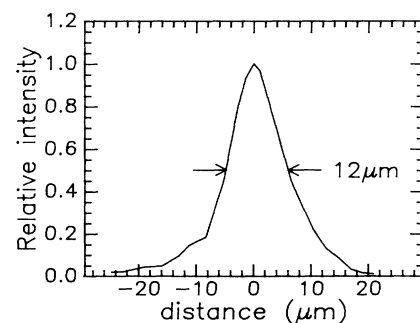
Measurements of the beam profile were obtained by means of a simple achromatic microscope which magnified and imaged any desired region of the focus onto a diode array or television camera. Using a 150-mm focusing lens, we obtained a focal waist with a full width at half maximum of  $12 \pm 2 \mu\text{m}$  with an approximate Gaussian profile (see Fig. 4). This value is near the diffraction limit for the system and corresponds to maximum peak intensities of  $\approx 10^{14} \text{ W cm}^{-2}$  in the focus.

Electron spectra in this experiment were accumulated over many laser pulses, so it was necessary to control the laser-intensity fluctuations from pulse to pulse. The light intensity was controlled by means of a  $\lambda/2$  plate and a polarizer at the laser output. (The final polarization was adjusted by an additional  $\lambda/2$  plate just before the focusing lens.) Energy fluctuations were stabilized by a feedback circuit to be less than  $\pm 2\%$  during a data-collection run.

### C. Vacuum requirements and space charge

It is important to maintain a clean vacuum chamber in ATI experiments because the high intensities are sufficient to ionize most vacuum-chamber contaminants. The interaction region in this experiment was housed in a small vacuum chamber maintained by a turbomolecular pump at a base pressure of  $6 \times 10^{-9}$  Torr. The xenon density was varied from  $2 \times 10^{-5}$  to  $4 \times 10^{-8}$  Torr by changing the rate of flow through a leak valve.

There are several factors which dictated the xenon density used in this experiment.

FIG. 4. 1064-nm beam profile at the focus measured with a  $12\times$  magnification and a CCD diode array with  $25 \mu\text{m}$  elements. A 15-cm ( $f/10$ ) lens was used to focus the beam.

(1) The microchannel plate electron detectors require vacuum better than  $1 \times 10^{-4}$  Torr.

(2) Pulse pileup in the electron counters can distort the spectrum.

(3) Xe pressure should be significantly greater than the base pressure of the chamber.

(4) Space charge distorts the electron energies if there is too much ionization.

Except at very low laser intensities, the last item is by far the most important. Many of the ATI measurements involve electron energies, spectral widths, and total yields, and all of these can be distorted by space charge. The use of a tight focusing geometry and minimum xenon densities served to reduce these effects. The focal volume for our laser was approximately  $10^{-7}$  cm<sup>3</sup>. At a pressure of  $10^{-5}$  Torr the number of particles in this volume is  $3 \times 10^4$ . The ions are essentially static during the laser pulse so that as the fast photoelectrons leave the interaction volume the remaining electrons see an increasingly attractive potential. For  $3 \times 10^4$  singly charged ions in a spherical region of  $10^{-7}$  cm<sup>3</sup> volume, an electron on the surface sees a potential greater than 1 eV. Thus the last electrons to leave the interaction region, that is the low-energy, slow electrons, can be significantly shifted in energy due to the attractive potential of the residual ions.

The effect of space charge on the xenon photoelectron spectra can be seen in Fig. 5, which displays data at two different xenon densities with all other experimental conditions identical. It is also a simple matter to model the effect of the ion potentials on the photoelectron spectra.<sup>3</sup> We have calculated the size and nature of space-charge effects for our geometry and found that space charge manifests itself through an asymmetric broadening and shift of the ATI peaks in the electron-energy spectrum, as well as a change in the angular distribution. These effects are most prominent for the low-energy electrons which are the last to leave the interaction volume. We established empirically, and verified by computer calculations, that space-charge effects were negligible with our collection geometry if the electron counting rate was kept below  $\approx 2$

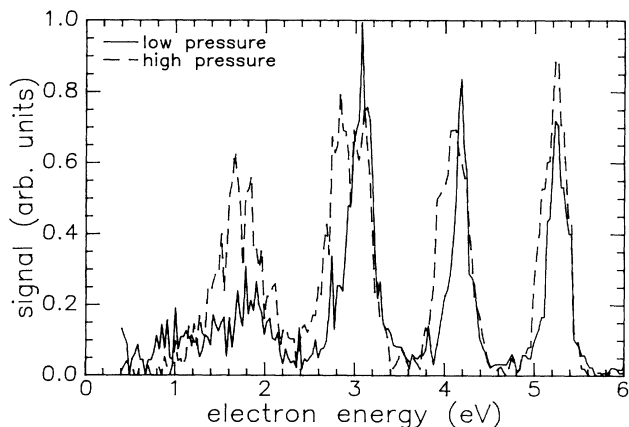


FIG. 5. Demonstration of space-charge induced broadening of the electron spectrum in xenon ATI. The solid line corresponds to xenon pressure of  $1 \times 10^{-7}$  Torr, and the dotted line is for  $8 \times 10^{-6}$  Torr.

electrons per laser shot when the polarization of the optical electric field was along the detection axis. This criteria was met by changing the xenon pressure in concert with changes in the laser-pulse energy. At sufficiently high laser energies, which result in a large effective volume for ionization, the space-charge effects from the vacuum vessel background gas could become sufficiently large to interfere with accurate measurements of the xenon photoelectron spectrum. This effect set the upper limit on the laser pulse energies used in the data reported here.

The use of low count rates also reduces the occurrence of pulse pileup in the time-of-flight electron spectrometer. The width of the electron spectral features in the time domain depends inversely on the energy of the electrons. Consequently when the electron counting rate is high enough that coincident electrons become significant, the lower-energy electron peaks are enhanced relative to higher-energy peaks. The criterion for eliminating space-charge effects also assured that pulse pileup was not a significant factor.

#### D. Spectrometer

The time-of-flight spectrometer consisted of a 2-cm-diameter, 40 cm long, magnetically shielded, tubular, copper Faraday cage. The shielding surrounded the interaction region and the focused light was introduced through 1-cm entrance and exit holes. Microchannel plate electron detectors at the end of the spectrometer tube subtended a  $3^\circ$  angle at the source ( $2 \times 10^{-3}$  sr collection solid angle). The signals were fed through an impedance-matched conical anode to the transient waveform digitizer with an overall time resolution of 2 ns. Stray fields limited the overall resolution to approximately 0.03 eV at an energy of 1 eV, and the resolution width increases roughly as the square root of the energy. A time-of-flight spectrum was recorded for every laser shot and single electron pulses were software discriminated and binned.

### III. DATA

Our studies of Xe and Kr ATI have concentrated on features of the electron spectra: the electron energies, spectral line shapes, angular distributions, and polarization effects. In this section we summarize our experimental findings.

#### A. Energy spectrum

The relevant energy levels in Xe and Xe<sup>+</sup> are shown in Fig. 6. The two ionization limits correspond to the fine structure of the Xe<sup>+</sup> ground state. Because of this splitting there are two threshold processes: absorption of 11 Nd:YAG photons to the Xe<sup>+</sup>  $^2P_{3/2}$  ground state with a 0.682-eV free electron, and 12-photon absorption to the Xe<sup>+</sup>  $^2P_{1/2}$  configuration with a 0.550-eV free electron. Absorption of  $S$  additional ATI photons will produce electrons having energies of  $Sh\nu + 0.682$  eV for the  $^2P_{3/2}$  final ion state and  $Sh\nu + 0.550$  eV for the  $^2P_{1/2}$  final state. These are total energies of the free electron and represent their kinetic energy outside the field.

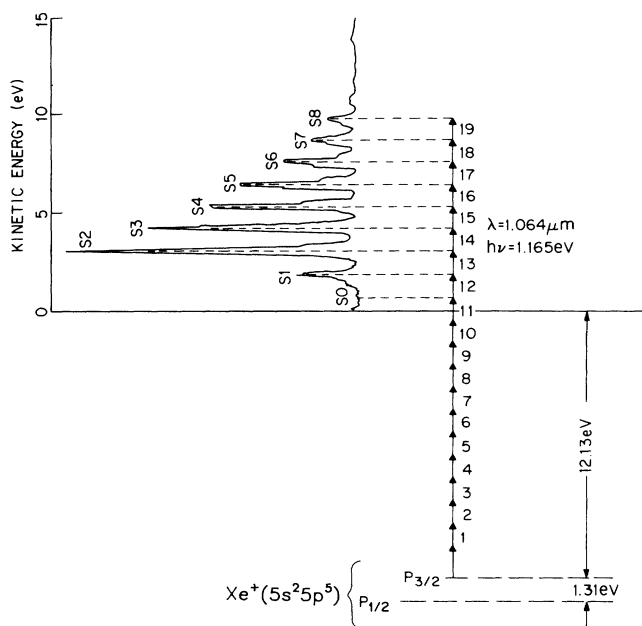


FIG. 6. Electron-energy spectrum corresponding to absorption of photons above the ionization threshold. Zero energy corresponds to a free electron at rest for either of the two ion-core configurations. The negative energy states represent the ionization energies for the two core configurations and they are thus inverted relative to the normal ion spectrum.

Figure 7 shows a number of Xe spectra at several laser intensities, with peaks for  $S=0-10$  or more. Each spectrum contains data of 2000–30 000 laser pulses. In these spectra as well as those of Figs. 8 and 9, the light was linearly polarized along the detector axis. In order to display them all on the same graph, they have been renormalized by scale factors as shown along the vertical axis. The  $^2P_{3/2}$   $S$  peaks should be separated from the  $^2P_{1/2}$   $S-1$  peaks by 0.132 eV. Unfortunately, the widths of the peaks for 1064-nm excitation are too broad to allow separate observation of these two series.

Similar data for Kr are shown in Fig. 8. In this case, the two fine-structure components of  $Kr^+$  produce elec-

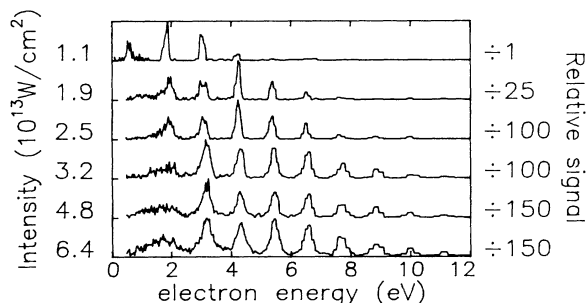


FIG. 7. Xenon photoelectron spectra for 1064-nm light. The polarization is linear, oriented along the detection axis. The rescale factor at right may be used to obtain the relative rates per unit xenon density.

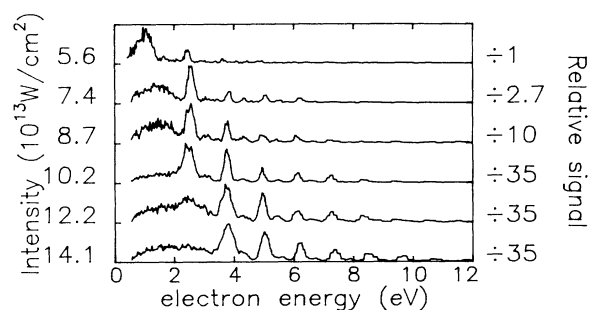


FIG. 8. Krypton photoelectron spectra for 1064-nm light, linearly polarized along the detection axis. The rescale factor at right may be used to obtain the relative rates per unit krypton density.

trons at  $Sh\nu+0.483$  eV ( $^2P_{1/2}$ ) and  $Sh\nu+1.148$  eV ( $^2P_{1/2}$ ), which are clearly resolved, allowing comparison of the yield to the two possible final ion states. If the rates were equal, one would expect a statistical ratio of  $(\frac{1}{2} \text{ yield}) : (\frac{1}{2} \text{ yield}) = 2$ , but clearly this is not the case for Kr. Fabre *et al.*<sup>4</sup> have reported relative intensities of the  $^2P_{3/2}$  and the  $^2P_{1/2}$  peaks in Xe at low intensities and noted that the expected 2:1 statistical ratio was not observed there either.

Data similar to Figs. 7 and 8 were first obtained by Kruit, Kimman, and van der Wiel<sup>5</sup> in 1981, and subsequently many authors commented on the absence of large Stark shifts in the peak positions.<sup>5-7</sup> There is now general agreement that the shifts, if any, are quite small in these experiments.

For excitation with 532-nm radiation the peaks are separated by 2.33 eV, with the  $S=0$  threshold peak in Xe occurring at 0.550 eV for the  $^2P_{1/2}$  final state and 1.817 eV for the  $^2P_{3/2}$  state. The peaks are separated sufficiently in energy that there is no overlap. Typical spectra are shown in Fig. 9; an alternation in intensity associated with the different final states is easily discernible, though it is not so dramatic as with the 1064-nm Kr spectra.

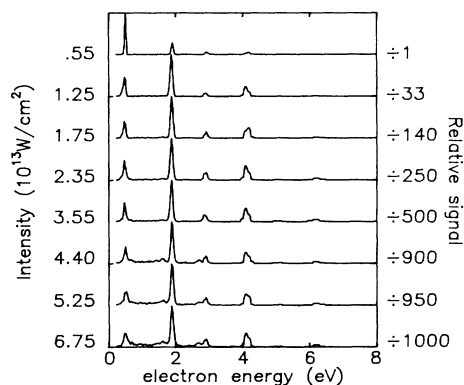


FIG. 9. Xenon photoelectron spectra for 532-nm light. The polarization is linear, oriented along the detection axis. The rescale factor at right may be used to obtain the relative rates per unit xenon density.

### B. Total ionization yields

The ionization rate increases extremely rapidly with laser intensity. This is expected for such a high-order process, and is dramatized in Figs. 7 and 8. The total number of photoelectrons contained within each ATI peak in Fig. 7 is shown as a function of the laser energy in Fig. 10. At low intensity, minimum-order perturbation theory predicts that an  $N$ -photon process should increase as  $I^N$ . Deviations from this simple prediction are expected for several reasons.

(1) The data are not integrated over all angles. The orientation for the data in Fig. 10 is with linearly polarized light along the detection axis. Thus any intensity-dependent angular distributions will distort the electron yield by diverting electrons away from the detector.

(2) Various saturation mechanisms may change the power-law dependence. Depletion saturation will reduce the observed power dependence. If the ionization potential changes appreciably in intense light fields, the threshold channel may be cut off which in turn may increase the

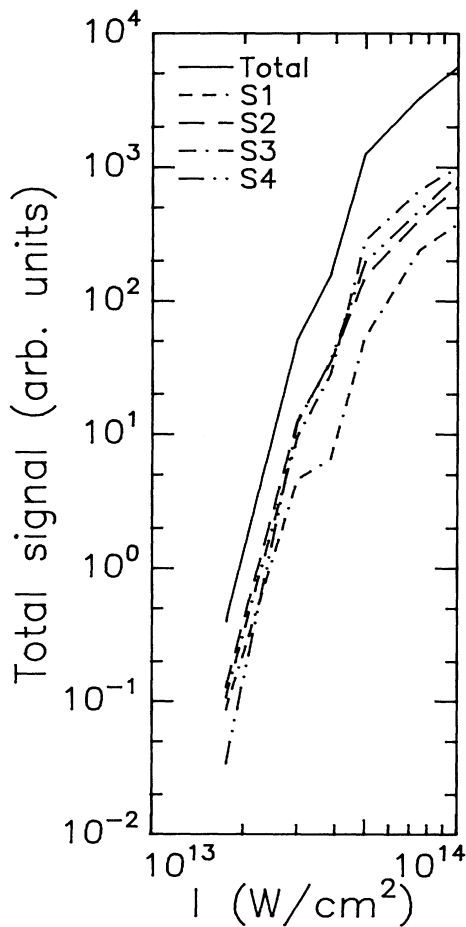


FIG. 10. Electron signal vs 1064-nm laser energy in xenon, for linearly polarized light along the detector axis. The integration is performed over the energy for each peak, to account for changing linewidths. The x axis shows the peak intensity of the laser pulse.

power dependence.

(3) At high intensities, lowest-order perturbation theory may be an inadequate description of the ionization process.

Much has been made in previous ATI experiments of the apparent disappearance of the low-energy electron peaks.<sup>6,7</sup> In Fig. 7, the  $S=0$  peak is only distinguishable at very low laser energies, well below the onset of saturation seen in Fig. 10. At higher laser intensities (with a concomitant reduction in the xenon density) the lowest-energy peak appears to broaden, while a continuum background increases to the point that it is much larger than the initial height of the  $S=0$  peak. We know that the small size of the  $S=0$  peak, and its subsequent indiscernibility within the background, is not the result of instrumental sensitivities because the  $S=0$  peak is observed to be a relatively prominent peak in spectra taken with 532-nm radiation (Fig. 5). Although the  $S=0$  peak is not discernible at higher intensities with 1064-nm excitation, the low-energy electrons must be present since the intensity history on axis at low pulse energies is duplicated by off-axis regions when the energy in the pulse increases. For a Gaussian spatial beam profile, the sample volume experiencing a given maximum intensity in its time history is a slowly but monotonically increasing function of the laser energy. This fact is evidently masked by the rapid increase in the background signal which hides the  $S=0$  peak in the noise. We therefore conclude that, in contrast to other published interpretations, *the low-energy electrons do not disappear in any absolute sense*, provided data is accumulated under conditions in which space charge plays no role.

The saturation behavior observed in Fig. 10 has been seen in several ion and electron ATI experiments. Many investigators<sup>4,6-9</sup> have made detailed studies of the order of nonlinearity from data of this type. In our plots, we see that at low energy the slope of the signal in both the  $S=1$  and 2 peaks, as well as the total electron signal, are all compatible with an  $I^{13}$  dependence on the laser intensity, although the uncertainty in the slope is large ( $\pm 2$ ). At a laser intensity of  $\approx 10^{13}$  W cm<sup>-2</sup> the slope decreases. This is termed the saturation intensity and has been measured by Lompre *et al.*<sup>7</sup> to be  $1.2 \times 10^{13}$  W cm<sup>-2</sup> for Xe for 1064-nm radiation. It is widely assumed that this saturation is caused by depletion of the ions in the focal volume, but this has not yet been firmly established. We have determined the saturation intensity from our angular distribution data and obtained a value of  $2.8 \times 10^{13}$  W cm<sup>-2</sup>. Our measurements, described below in the discussion of angular distributions, differs from Lompre *et al.* in that it does not depend on either energy measurements or precise beam-profile measurements. At intensities below saturation, the spectrum is dominated by the low-energy electron peaks. As the intensity increases, the higher-energy electron peaks become increasingly prominent as shown in Fig. 10. Increasing the laser intensity above saturation tends to broaden the peaks, especially the low-energy ones, and to increase the size of all the peaks with little effect on the relative sizes. The increase in the total signal above the saturation intensity is due at least in part to the increase in the effective interaction volume.

### C. Linewidths

A striking feature of the photoelectron spectra is the intensity-dependent widths of the ATI peaks. Kruit *et al.*<sup>6</sup> first pointed out that the widths of the ATI peaks were significantly larger than the instrumental linewidths and depended on the wavelength of the excitation laser. Table I shows measured linewidths for Xe and Kr peaks produced with 1064 and 532-nm radiation in our experiments. For both Xe and Kr the widths of the peaks produced with 532-nm radiation are significantly less than the widths produced with 1064-nm radiation. For 1064-nm the peaks in Kr are wider at high laser intensity than in Xe. Since the saturation intensity for Kr is higher than for Xe, the photoelectrons are presumably produced at higher fields in Kr than in Xe. In the case of Xe the widths of the spectral peaks prevents the observation of separate fine-structure features. The two channels are offset by 0.666 eV in krypton with 1064-nm excitation and are easily resolved.

At high intensities the broadening of the photoelectron peaks is accompanied by a large increase in the level of "background" electrons. While these electrons may represent the wings of the individual peaks, the absence of any knowledge of the true line shapes makes it difficult to establish the number of electrons within each ATI peak. This is far more serious at 1064-nm than at 532-nm both because of the larger linewidths and the decreased spacing between peaks.

### D. Angular distributions

The angular distributions of photoelectrons in multiphoton ionization (MPI) provide valuable information about the atomic physics of the multiphoton transitions, and are potentially among the most valuable measurements to compare with theory. Measurements have been reported on the low-intensity angular distribution of photoelectrons produced in ATI studies of Xe using both 1064- and 532-nm radiation.<sup>11</sup> However, MPI occurs at such high intensities that there are significant effects of the light field on the photoelectrons after ionization.<sup>12</sup> The ponderomotive forces act on free electrons in the direction of the negative intensity gradient. Thus the observed angular distributions are expected to vary not only with ATI order, but also with the intensity of the laser light and its associated beam profile.

In our studies,<sup>13</sup> the angular distributions were obtained by detecting electrons at right angles to the incident radiation and rotating the polarization direction in the plane containing the detector. Figure 11 shows polar plots of the intensity for the  $S=1, 2,$  and  $3$  peaks in xenon as a function of laser intensity for 1064-nm light. (The electron signal is plotted as a function of the angle between the polarization direction and the detection direction.) The distribution is highly peaked along the direction of the polarization at the lowest intensities, with the ratio of the number of electrons observed along the polarization to that normal to the polarization being greater than 5 for  $S=1$ , and greater than 10 for  $S=2$  and  $3$ . The angular distribution becomes increasingly isotropic as the laser intensity is increased, reaching a ratio between maximum and minimum signal strengths of  $\approx 1.2$  for  $S=1$  at the highest laser intensities. The isotropy for  $S=2$  and  $3$  at high laser intensities is not so pronounced, but it is still considerably more than that observed at low intensities. Threshold ( $S=0$ ) electrons could not be observed at intensities above saturation, so their angular distributions were not recorded.

Special care was taken in these measurements to insure that these intensity distributions were not an artifact arising from space charge. In addition to the precautions concerning space charge discussed above, all of the angular distribution data reported here were taken over a wide range of xenon densities to establish any dependence of the angular distributions upon the number of ions created

TABLE I. Full width at half maximum (FWHM) in eV for photoelectron spectral peaks. Estimated combined statistical and systematic error of 0.05 eV.

Maximum intensity ( $10^{13}$ W/cm <sup>2</sup> )	Xenon ionized by 1064-nm light (from Fig. 7)						
	Peak designation						
	S1	S2	S3	S4	S5	S6	S7
1.1	0.18	0.16	0.16	0.17			
1.9	0.82	0.32	0.27	0.15	0.17	0.14	
2.5		0.41	0.26	0.20	0.22	0.19	0.29
3.2		0.77	0.40	0.28	0.25	0.27	0.32
4.8		1.15	0.43	0.31	0.28	0.30	0.36
6.4		1.10	0.52	0.46	0.35	0.35	0.36
Maximum intensity ( $10^{13}$ W/cm <sup>2</sup> )	Krypton ionized by 1064-nm light (from Fig. 8)						
	Photons absorbed						
	13	14	15	16	17	18	
5.6	0.59	0.24					
7.4	1.18	0.27	0.22	0.24	0.30		
8.7	1.26	0.38	0.22	0.34	0.30		
10.2	1.5	0.48	0.23	0.20	0.23	0.25	
12.2	2.4	1.05	0.42	0.27	0.31	0.35	
14.1		2.5	0.52	0.35	0.30	0.35	

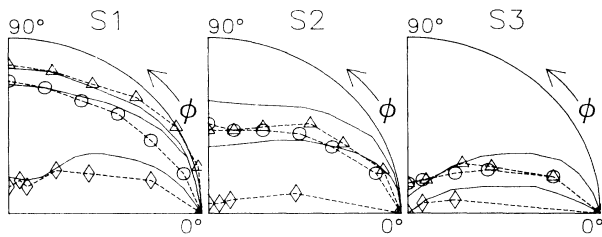


FIG. 11. Azimuthal angular distribution data and calculations for peaks S1, S2, and S3 as a function of intensity. The experimental laser peak intensity was  $1.5$ ,  $3.0$ , and  $6.0 \times 10^{13}$  W/cm<sup>2</sup> for data represented by diamonds, circles, and triangles, respectively. The results of the model calculations invoking ponderomotive scattering are shown as solid lines. The calculations were performed for the same laser intensities as the data, except that calculations were not performed for the lowest laser intensities for S2 and S3 electrons. The data show how the ponderomotive force affects the slower electrons more than the faster ones.

in the ionization pulse. Provided the count rate remained below our empirically determined limit of 2 counts/shot (along the polarization direction), we found *no* dependence of the angular distributions on the number of xenon ions.

Before measurements of the angular distributions were made, the optics of the focusing system were measured and adjusted to insure that the focus contained an axially symmetric light beam. The beam focus was imaged onto a television camera and monitored throughout these measurements to guard against any changes in laser mode, position, or quality of focus.

#### E. Effect of spatial beam profile on electron trajectories

The intensity dependence of the angular distributions is postulated to arise from scattering of the free electrons by the ponderomotive potential of the large fields of the laser within the focus, as explained in detail below. A direct experimental test for the presence of this scattering is to check whether the electron angular distribution depends explicitly upon rotations of an asymmetric spatial pattern of the laser intensity. We created an asymmetric field pattern at the focus by aperturing the laser beam by 50% in one dimension with a slit just before the focusing lens. This resulted in an increase in the width at the focus by approximately a factor of 2 in that dimension. The change in shape at the focus from a circular cross section normal to the direction of propagation to an elliptical cross section was verified by observing the magnified image in the microscope-television camera. The laser polarization  $\epsilon$  was oriented along the major axis of the ellipse, so that the photoelectrons, which are preferentially emitted along  $\epsilon$ , would scatter maximally. The orientation of the ellipse was then rotated, keeping  $\epsilon$  along the major axis, in order to observe the angular distribution of the electrons leaving the focus. The results, shown in Fig. 12, show the strong effect of the ponderomotive potential in distorting the angular distribution. In striking contrast to Fig. 11, the angular of maximum electron intensity is now

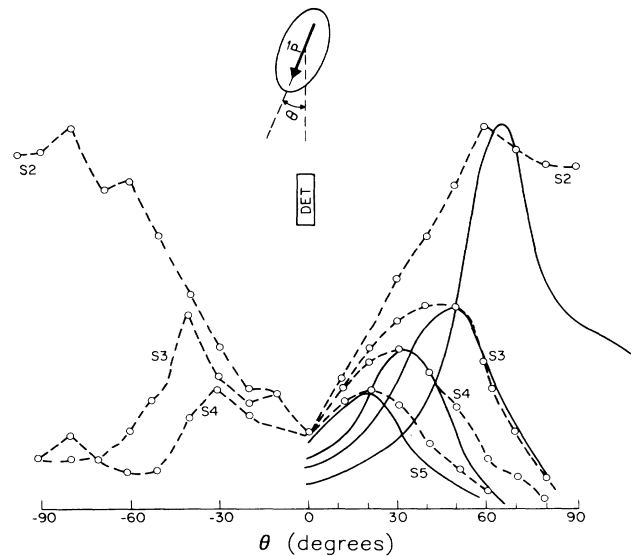


FIG. 12. Experimental distribution of photoelectrons as a function of angle from the direction of the axis of the ellipse with a 3:1 eccentricity with the axis of the ellipse parallel to the electric field polarization. Here the ponderomotive force is no longer cylindrically symmetric, being strongest along the minor axis of the ellipse. Also shown are the results of the model calculation using parameters determined from the circular focus fits. The calculation has been normalized in height for each SN peak.

along the greatest intensity gradient (along the minor axis) which is normal to the polarization vector.

#### F. Effect of laser polarization

Most ATI experiments have been performed with linearly polarized light, whereas most theoretical treatments of ATI involve circularly polarized light. In very-high-order nonresonant MPI, the major difference between these two cases is the large amount of angular momentum which must be carried off by the photoelectron after it has absorbed many circularly polarized photons. Figure 13 shows the photoelectron spectrum using circularly polarized 1064-nm light, detected in the polarization plane. Figure 14 shows circularly polarized 532-nm spectra. The effect of using circular polarization is most easily seen by comparing Fig. 13 with Fig. 7, which shows 1064-nm linearly polarized spectra. In addition to the  $S=0$  peak, the  $S=1-4$  peaks are absent for circular polarization. This suppression of the low-energy peaks is essentially independent of laser energy above saturation, and persists up to the highest intensities used. The small number of low-energy electrons which were detected is consistent with ionization of background gas and small imperfections in the circular polarization.

As shown in Fig. 11, the angular distribution of the photoelectrons is highly peaked along the polarization direction when linearly polarized light is used. With circularly polarized light the photoelectron distribution is uniformly distributed in the plane normal to the propaga-

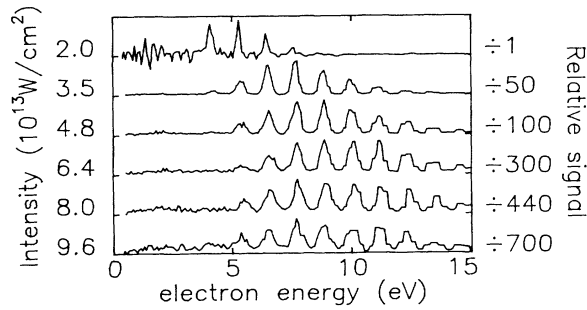


FIG. 13. Photoelectron spectrum for circularly polarized 1064-nm laser radiation in xenon.

tion vector of the light and the angular acceptance of the electron detector is  $\approx 0.05$  rad in this plane. The ratio of the peak photoelectron signals for linear and circular polarization at saturation is consistent with this acceptance angle and these angular distributions. A lower cross section for ionization using circular polarization shows itself in the higher intensity necessary for saturation. This has been reported earlier in studies of total photoionization yields.<sup>8</sup>

For Kr the suppression of low-energy electron peaks by circularly polarized light is masked by the large number of continuum electrons, but the overall effect is the same as in Xe.

#### IV. ANALYSIS AND DISCUSSION

The rich variety of phenomena observed in ATI experiments generally fall into two categories of light-matter interactions: photon absorption and photon scattering. Absorption is observed through ionization, in this case MPI and ATI; scattering processes include Stark shifts, ponderomotive forces, light pressure, Thomson scattering, and a range of nonlinear phenomena which derive from the interaction of photons with “dressed states,” i.e., with matter under the influence of intense light. The boundary between these categories is not always distinct. Stark shifts can enhance or suppress MPI rates; stimulated scattering can transfer energy between light and matter, as can Compton scattering. But in a quantum picture, the

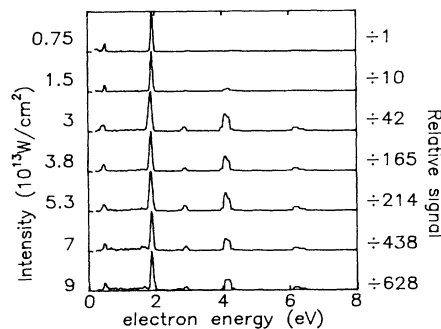


FIG. 14. Photoelectron spectrum for circularly polarized 532-nm laser radiation in xenon.

difference is that absorption processes remove photons from the radiation field, while scattering processes merely change their quantum state.

In weak laser fields, the effects of scattering on ionization spectra are small, and have traditionally been ignored. However, the effect of light scattering in its manifestation as ponderomotive forces has been extensively discussed in studies of low-density plasmas.<sup>12,14</sup> Here we show how ponderomotive forces can help explain many of the effects observed in ATI spectra.

#### A. Photoelectron energy spectrum

An atom irradiated by quasimonochromatic radiation at frequency  $\nu$  can absorb energy only in units of  $h\nu$ . Ionization is defined as the transition to a state where the electron can move far enough from the residual ion that its motion is unaffected by the field of the ion. It is necessary to define ionization in this way rather than in terms of energies since the free electron can have substantial energy in the presence of the radiation field even when its average velocity is zero.

Conservation of energy is sufficient to show that the photoelectron spectrum must consist of discrete peaks whose positions are independent of any of the details of the ionization process except the ground-state energy levels of the atom and ion. Specifically, the positions of the electron peaks cannot depend on any shift of the ionization potential.<sup>15</sup> If  $E_{GS}$  and  $E_{ion}$  are the atomic ground-state and ion final-state energies, including kinetic energies, in the absence of a laser field then the final electron kinetic energy outside the field,  $E_{kinetic}$ , is given by energy conservation,

$$nh\nu + E_{GS} = E_{kinetic} + E_{ion} \quad (1)$$

In intense fields,  $E_{kinetic}$  can only shift as the difference  $E_{ion} - E_{GS}$ . This shift represents the work done by the field on the atom as it enters the focus, minus the work done as the ion exits. This net energy change is equal to the difference of the Stark shifts of the initial neutral ground state and the ion final state. Except for this, energy is conserved. (Note that this argument only holds for steady-state laser beams, and must be altered if the laser pulse is short compared to the transit time of the photoelectron through the focus.) If there is more than one initial or final state, it will be reflected in more than one value for  $E_{GS}$  or  $E_{ion}$  and correspondingly a more complex energy spectrum. Thus the spectrum of the photoelectrons does not depend on the behavior of the excited states of the atom in the field nor on the details of the process of photoionization.

#### B. Ponderomotive potential

Since conservation of energy and momentum preclude absorption of photons by free electrons, their only interaction is through scattering. At low intensities and for optical frequencies this is Thomson scattering, with cross section  $\sigma_T = 0.665 \times 10^{-24}$  cm<sup>2</sup>. For high laser intensities, however, the cross section is significantly enhanced by stimulated processes and corresponds to the classical pro-

cesses known as ponderomotive effects. These produce a force along the negative gradient of the intensity of the field that is independent of the direction of polarization of the radiation. The ponderomotive force of a radiation field on a free electron was considered by Kapitza and Dirac, although antecedents exist as far back as the early work of Lord Kelvin.<sup>16</sup>

The ponderomotive force in our experiments can be understood either from classical equations of motion<sup>14</sup> or by considering the Schrödinger Hamiltonian for a free electron in the presence of a classical radiation field.<sup>17</sup> The Schrödinger Hamiltonian is

$$H = \frac{\left[ \mathbf{p} - \frac{e}{c} \mathbf{A}(\mathbf{r}, t) \right]^2}{2m_e}, \quad (2)$$

where  $\mathbf{A}(\mathbf{r}, t)$  is the classical periodic vector potential for the laser beam. If the numerator of  $H$  is expanded and averaged over an integral number of cycles of  $\mathbf{A}$ ,  $H$  can be rewritten as

$$\langle H \rangle = \frac{p^2}{2m_e} + \frac{e^2 A^2(\mathbf{r})}{4m_e c^2}. \quad (3)$$

The second term appears as a repulsive potential for the electron. When expressed in terms of the fields rather than the vector potential, this is

$$V = \frac{e^2 E^2}{4m_e \omega^2}, \quad (4)$$

which is just the average kinetic energy of an electron in an oscillating electric field  $E \in \cos(kx - \omega t)$ . Thus this effective potential is actually caused by the oscillatory "wiggle" motion of the particle in response to the driving force of the radiation field.

The total energy is the oscillatory energy  $E_p$  plus the directed kinetic energy.<sup>14</sup> If a free electron travels from a region of low intensity to a region of higher intensity, its directed kinetic energy is converted to oscillatory energy. The highest-intensity region into which the electron can penetrate is one in which the stored oscillatory energy equals the initial kinetic energy outside the beam. Conversely, if a free electron is initially in a radiation field it will have an oscillatory energy given by Eq. (4) and as it leaves the beam this will be converted to directed kinetic energy and added to any directed kinetic energy which it initially had. A free electron starting in an intense light beam will reach the detector with at least as much energy as the ponderomotive potential in the region where it was produced. Thus the minimum energy of the photoelectrons and the associated minimum number of photons absorbed increases as  $E_p$  increases. In other words, the ionization potential of the atom is increased by the ponderomotive potential. This result is independent of any considerations of the details of the ionization, because the ionization potential must be equal to the energy of a free electron at rest, plus the energy of the final-state ion. Since the electron gains ponderomotive potential energy in the laser field, the ionization potential must also gain the same energy. (This agreement assumes that the ground-state energy minus the final-state ion energy does not shift

to track the ponderomotive potential of the free electron, an assumption that will be shown below to be generally true.)

The physics is perhaps more clear if the process is viewed in reverse. The reversibility of the equations assures that if photoionization is allowed, then the reverse process of recombination is allowed. Consider an electron at the detector having the kinetic energy corresponding to threshold ionization and an intense light beam so that  $E_p > h\nu$  at the ion. As the electron moves back towards the ion in the light beam, it moves into the conservative ponderomotive potential and converts its directed kinetic energy into oscillatory energy. Because its initial energy is less than  $E_p$  at the ion, it will come to rest and be repulsed before reaching the ion. Thus the recombination process cannot occur for electrons with initial energies below  $E_p$ . In a similar manner, for a neutral atom in the intense field, absorption of the minimum number of photons to remove the electron from the Coulomb well of the nucleus will not be sufficient to also raise the electron to the level of the potential hill produced by the ponderomotive interaction. Thus the electron must remain in the neighborhood of the ion until it has absorbed additional photons. When it does escape as a free electron it will be detected in one of the higher-energy channels given by Eq. (3).

### C. Ground-state Stark shifts

The energy spectrum of the photoelectrons as given by Eq. (1) depends on the difference in the Stark shifts of the ground state of the neutral atom and the ion in the optical field. For a well-defined light intensity a large difference in the neutral and ion Stark shifts would manifest itself in a shift of the photoelectron-energy spectrum. For those experiments where well-defined ATI spectra such as shown in Fig. 7 exist, the spectra themselves can be taken as evidence that large Stark shifts of the ground state are not present. For cases where the photoelectron spectrum is continuous, large Stark shifts may be the origin of the continuum, although there may be other causes as well for the energy distributions.

Classically, the ac Stark shift is the increase in the energy of a bound system due to dipole oscillations induced by the applied field. For a given driving force below resonance, a classical dipole will gain oscillatory energy inversely proportional to its spring constant. So we expect a more tightly bound system to have a smaller Stark shift. The size of the Stark shift in the ground state of xenon can be derived from the polarizability  $\alpha$ , which in turn may be obtained from the index of refraction at the driving frequency. A perturbation treatment was recently performed by Pan *et al.*,<sup>18</sup> who showed that for the ground state the second-order contribution of the  $epA/m_e c$  term in the atomic Hamiltonian almost exactly cancels the  $e^2 A^2/2m_e c^2$  contribution leaving a residual shift for the ground state of  $-\frac{1}{2}\alpha E^2$ . The residual shift is equivalent to the dc Stark shift with  $\alpha = e^2 \sum_n [ |\langle n | x | g \rangle|^2 / (E_n - E_g) ]$  being the ground-state polarizability. Here the summation is over all excited states,  $x$  is the projection of the electron coordinate on the polarization vector of the light, and  $E_n$  is the energy of the polar state  $\langle n |$ . Using the

Thomas-Reiche-Kuhn sum rule, the ac Stark shift can be shown to be less than  $e^2 E^2 / 4m_e \omega_r^2 = V(\omega^2 / \omega_r^2)$  where  $\omega_r$  is the frequency of the resonance transition,  $\omega$  is the optical driving frequency, and  $V$  is given by Eq. (4). For Xe the measured ground-state polarizability<sup>19</sup> is  $4.01 \times 10^{-24}$ , giving a ground-state Stark shift of 0.11 eV at an intensity of  $1 \times 10^{13}$  W cm<sup>-2</sup>. The Stark shift of the ion will partially cancel this shift in a calculation of the effect on the photoelectron spectrum.

#### D. Time-dependent ponderomotive potentials

The ponderomotive potential is only a conservative potential if the light field is "static," i.e., continuous wave. Since all ATI experiments involve pulsed lasers, time-dependent ponderomotive potentials are inherent in any measurements. This problem was considered in general by Kibble<sup>20</sup> and has been considered for its specific application to ATI by Hollis<sup>21</sup> and by Fiordilino and Mittleman.<sup>22</sup> If the intensity change is slow over a single cycle (this is true for all but the shortest laser pulses currently available) then the time-averaged Hamiltonian of Eq. (3) applies, allowing  $A^2(\mathbf{r})$  to be replaced with the slowly varying envelope of the vector potential  $\langle A \rangle^2(\mathbf{r}, t)$ . In this case a particle solution to Schrödinger's equation maintains its *momentum* in a time-changing potential, while its *energy* changes by the change in the potential  $V(t)$ . It is clear that if an electron has no momentum so that all of its energy is oscillatory energy and the intensity of the radiation field increases, then the energy of the electron must also increase. Conversely a decrease in the radiation intensity will decrease the electron energy. These effects have recently been observed in electron scattering from a focused laser beam.<sup>23</sup>

In the experiments reported here, the ponderomotive potential changes only a little during the passage of the electron out of the beam. A 1-eV electron has a velocity of  $6 \times 10^7$  cm/sec and will leave a 10- $\mu$ m focus region in at least 16 ps. Electrons with trajectories which are not directed radially outward will take significantly longer to leave the beam. This is enough to broaden the energy distributions, and the magnitude of the effect will depend on precisely where ionization occurs. Electrons which are produced on the leading edge of the radiation field and follow a trajectory which sees the intensity rise before they have left the beam will have their total energy increased. On the other hand, electrons made during the peak of the pulse and which do not leave the beam before the intensity has dropped will have a decrease in total energy. Thus a rapidly changing radiation field can both shift and broaden the photoelectron peaks. The model used in calculating the photoelectron trajectories included the dynamics of the light beam and was also used to predict the photoelectron widths.

#### E. Angular distributions

In experiments where the intensity changes very slowly compared to the passage of electrons out of the focus, the ponderomotive potential is nearly conservative. In experiments with rapidly changing intensities the broadening of the photoelectron peaks leads to a continuum energy dis-

tribution. In either case it is difficult to make direct observations of the ponderomotive interaction in the energy spectrum. On the other hand, momentum transfer during elastic scattering is quite strong, even when the energy peaks are relatively unaffected.

In our experiments described above it was found that the angular distribution of the photoelectrons is intensity dependent.<sup>13</sup> Furthermore, if the focus is made to be non-circular, the angular distribution depends on the shape of the focus and for a given shape it depends on the orientation of that shape. This is clear evidence that the trajectories of the photoelectrons is affected by the radiation field through which they pass after they are produced. To test the predictions of the ponderomotive interaction quantitatively, we constructed a computer model of the ponderomotive potential, and the ionization process in our laser focus. The model is based on the following physical assumptions.

(1) The initial angular distribution of the electrons is assumed to be intensity dependent and equal to values we measured at low intensities; about 12° opening angle about the polarization direction for the lowest ATI peaks down to 4° for the higher peaks.

(2) As a result of the highly nonlinear nature of the ionization, the atoms tend to ionize with a narrow range of intensities, so the electrons of a given ATI peak are assumed to be produced uniformly along equal intensity surfaces of the focused beam.

(3) The initial kinetic energy of the electrons is assumed to be  $E_{\text{init}} = E_{\text{final}} - E_p$ , where  $E_{\text{final}}$  is the detected energy and  $E_p$  is the value of ponderomotive potential at the intensity at which the electrons are created via ionization.

(4) The radial light distribution at a distance  $z$  from the focus is taken to be

$$I(r, z, t) = \frac{I_0}{r(z)^2} e^{-[r/r(z)]^2} e^{-[(t-z/c)/\tau]^2}, \quad (5)$$

where  $r(z)^2 = w^2 [1 + (\lambda z / \pi w^2)^2]$ ,  $\tau$  is the pulse length, and  $w$  is the spot size at the focus. The values for  $w$ ,  $I_0$ , and  $\tau$  were determined by direct measurement; an intensity of  $1 \times 10^{13}$  W cm<sup>-2</sup> yields a ponderomotive potential of 1.04 eV for 1064-nm radiation. The radial force resulting from (5) is proportional to

$$F(r, z, t) \approx \frac{2r}{r(z)^2} I(r, z, t). \quad (6)$$

Note that this force does not depend upon the polarization or the direction of propagation of the laser beam, but does depend on time.

The trajectories of a large number of electrons throughout the confocal volume were computed using Eq. (6), and the angular distribution for each ATI peak was calculated by averaging over the final angles of all the electrons. The only unknown in this simulation was the value of the intensity at which the electrons in each ATI peak were created: this one number was adjusted for each ATI peak for the best fit to the data at one intensity. The angular distributions for each ATI peak at all other intensities were calculated without further adjustment of any parameters. The results, which are in substantial agree-

ment with the data, are shown in Fig. 11.

The ATI peaks  $S=1, 2,$  and  $3$  have final energies of 1.6, 2.7, and 3.8 eV, respectively; the corresponding values for  $E_p$  obtained from fitting the data are 1.5, 2.6, and 2.8 eV. The various ATI channels have about the same saturation value of laser intensity, approximately  $2.8 \times 10^{13} \text{ W cm}^{-2}$  (2.7 eV) as determined from our data. For these channels the saturation intensity is also the intensity at which most of the electrons are made, and this determines the value of  $E_p$  for  $S=3$  and above. However, electrons cannot be made at an intensity corresponding to a ponderomotive energy greater than the corresponding  $E_{\text{final}}$ , as discussed before. Thus  $S=1$  and  $2$  electrons will be created (at a substantially reduced rate) at the highest intensity at which these channels are still open, namely, at a value of  $E_p$  which is slightly less than  $E_{\text{final}}$ .

This model provides a value for the saturation intensity which is independent of any intensity measurements of the laser beam, and is relatively insensitive to measurements of the beam profile. The saturation intensity follows from observing the angular distribution of electrons with different total energies and deducing their initial momentum. Our determination of the saturation intensity thus only depends on knowing the electron energy, which follows from knowledge of the energy levels of Xe, and the angular distributions. Our value is approximately 2.4 times the value determined by Lompre<sup>7</sup> by studying changes in the slope of the ionization curve.

The model was also used to predict the angular distribution of the ATI peaks from an elliptical focus, where the ponderomotive force is not axially symmetric. All of the relevant beam parameters were directly measured, and the angular distributions for the case of the light polarization along the major axis were measured. Figure 12 shows the results of the angular distribution measurements along with the predictions of the model computed without any adjustable parameters (i.e., using the same values for  $E_p$  obtained in the circular beam spot measurement). The model simulations satisfactorily reproduce the distorted angular distributions. In further experiments using the elliptical beam, we again found that if the polarization direction is kept fixed, then a rotation of the axes

of the polarization rotates the angular distribution of the photoelectrons.

#### F. Effects of circular polarization

The ATI results with circularly polarized light display markedly different features than for linear polarization, with higher average photoelectron energies, lower yields, and a virtual absence of low-energy electrons. It seems clear that ponderomotive forces cannot explain this difference, since for a given laser intensity, the ponderomotive potential is exactly the same for circular and linear polarization. We believe the explanation lies in the ionization process, and particularly in the fact that a photoelectron produced in circularly polarized MPI carries off nearly all the angular momentum absorbed from the laser beam. This places it in a continuum state with a large classical impact parameter that cannot easily overlap the ground-state atomic wave function. This explanation for the effect of circularly polarized radiation on the photoelectron spectrum has been presented elsewhere<sup>24</sup> and is only summarized here. The general argument is based on the spatial overlap of the initial ground electron state and the final continuum electron state. To allow for a direct comparison with experimental results we will restrict the treatment to a consideration of lowest-order perturbation theory only.

If the number of photons necessary to reach the ionization threshold is  $n$ , the first term in the perturbation expansion which contributes to the ionization is the  $n$ th-order term. If the angular momentum of the ground state is  $J$  and that of the final state is  $J'$ , then the angular momentum of the free electron, when ionized using circularly polarized light, is  $j \geq n - (J + J')$  and the orbital angular momentum is  $l \geq n - (J + J') - \frac{1}{2}$ . For the rare gases,  $J=0$  and  $J'=\frac{1}{2}$  or  $\frac{3}{2}$ , and the free electron produced by circularly polarized light is in a state of high angular momentum. On the other hand, if linearly polarized radiation were used, there need be no change in angular momentum on absorption of a photon, so the ionized electron could well have a low value of angular momentum.

The matrix element  $M$  is

$$M = (eE)^n \sum_{i_1} \cdots \sum_{i_{n-1}} \left[ \frac{\langle \psi_f | d^+ | i_{n-1} \rangle \cdots \langle i_1 | d^+ | \psi_0 \rangle}{\delta E_{n-1} \cdots \delta E_1} \right], \quad (7)$$

where the initial, intermediate, and final states are  $|\psi_0\rangle$ ,  $|i_m\rangle$  and  $|\psi_f\rangle$ , respectively;  $\delta E_i = E_i - E_0 - m\hbar\omega$  are the detunings associated with the intermediate states; and  $E$  is the electromagnetic field strength. For a high-order nonresonant process, no single intermediate states dominate the sum, and therefore the detunings  $\delta E_i$  may be replaced by a single value  $\delta E$  representing an average-energy denominator, which may then be removed from the sum.<sup>25</sup> The sum may then be carried out over the complete set of intermediate states, reducing  $M$  to

$$M \approx \frac{(eE)^n}{(\delta E)^{n-1}} \langle \psi_f | (d^+)^n | \psi_0 \rangle. \quad (8)$$

The high angular momentum final states are hydrogenlike continuum wave functions which see a central Coulomb potential plus a centrifugal repulsion

$$V_{\text{eff}}(r) = \frac{-1}{r} + \frac{l(l+1)}{2r^2}. \quad (9)$$

The value of the matrix element  $M$  depends on the over-

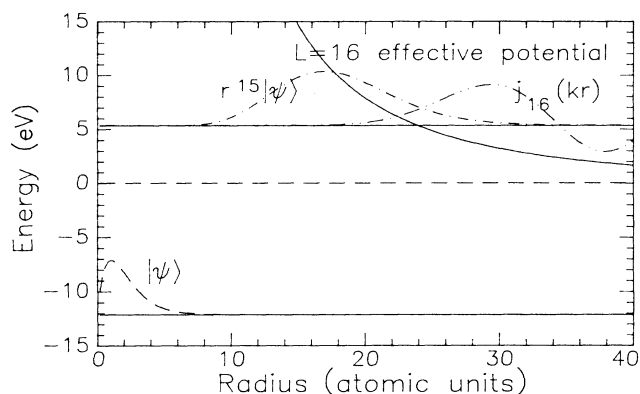


FIG. 15. Effective potential  $V_{\text{eff}}$  and final-state continuum wave functions for angular momentum  $l=16$  superimposed on the ground-state radial wave function  $\psi$  and  $r^{15}|\psi\rangle$  for xenon. The poor overlap demonstrates how the centrifugal barrier can suppress the production of low-energy electrons in photoionization with circularly polarized light.

lap of the final-state wave function with the ground-state wave function  $r^n\psi_0$ . This has a maximum probability density localized in a region around  $r=na_0$ , where  $a_0$  is the Bohr radius. Figure 15 shows the initial- and final-state wave functions for threshold MPI, and for the  $S=4$  ATI process in xenon. Just above ionization threshold the angular momentum barrier keeps the low-energy electron out at sufficiently large  $r$  that there is little overlap with the ground state, and  $M$  is very small. For higher-order peaks the free electron energy rises rapidly and there is progressively more penetration. In addition, the function  $r^n\psi_0$  peaks at progressively larger  $r$  for larger  $n$  and the result is increasing overlap. Thus the radial matrix element in Eq. (8) produces a suppression of low-energy photoelectrons because of the high angular momentum which the outgoing electron must carry off after absorbing so many photons. The coefficient  $(eE)^n/\delta E^{n-1}$  tends to

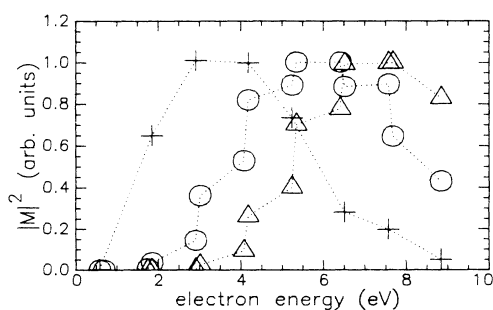


FIG. 16. Variation of  $|M|^2$  between the initial  $|5p\rangle$  state and final  $|E_n\rangle$  continuum state in xenon, corresponding to  $n$  photon absorption to the  $(\frac{3}{2})$  final state ion.  $E_n = nh\nu - E_i$  is the free electron energy where  $E_i$  is the ionization energy. Angular momentum of continuum state is  $l=n+1$ , and  $E_i$  includes both  $\text{Xe}^+$  final states. (+),  $h\nu=532$  nm; (O),  $h\nu=1064$  nm; ( $\Delta$ ),  $h\nu=1064$  nm, with a ponderomotive potential of 1 eV.

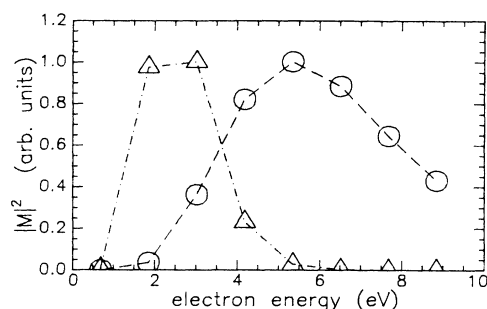


FIG. 17.  $|M|^2$  as described in Fig. 16, for ( $\Delta$ ),  $eEa_0/\delta E=0.068$  (estimate for Ref. 24); (O),  $eEa_0/\delta E=0.2$  (Ref. 26).

have the opposite effect: the rate for successively higher electron peaks corresponding to absorption of an additional photon is suppressed by a factor approximately equal to  $(eEa_0/\delta E)^2$ .

Figure 16 shows the results of calculations of  $M^2$  for Xe using Bates-Damgaard ground-state wave functions and spherical Bessel functions for the high-angular-momentum continuum states. The calculations match the experimental results well with the value of  $E/\delta E=0.2$  chosen to match the relative values of the high ATI peaks. Note there is little suppression of peaks when 532-nm radiation is used. The calculations for Fig. 16 included the effect of the ponderomotive potential on the kinetic energy of the free electron.

Lower-energy electrons did appear in circular polarization ATI experiments carried out by Yergeau, Petite, and Agostini<sup>26</sup> at intensities reduced from ours by approximately a factor of 10. This reduces the electric field in Eq. (2) by the square root of 10. The equation then yields relative sizes for the matrix element shown in Fig. 17. Although the lowest peak is still suppressed this shows that at low intensities, the nonlinear electric field dependence of different electron peaks can dominate the centrifugal suppression for circularly polarized light, resulting in the appearance of low-energy electrons in the spectrum.

## V. CONCLUSION

Much is now understood about the phenomena surrounding above-threshold ionization, but some important puzzles remain.

(1) Stimulated scattering plays a major role in most ATI experiments. The situation is most clear for final-state effects, where intensity-dependent angular distributions in ATI photoelectron spectroscopy can be satisfactorily reproduced with the simple model for the generation and subsequent propagation of free electrons in the ponderomotive potential of the laser focus.

(2) The ponderomotive potential also helps to explain the relative suppression of low-energy electrons in linear polarization ATI experiments. Other saturation mechanisms may also exist, however. The order of nonlinearity in the transition rates to individual electron peaks is not understood, and much experimental and theoretical work may center on the issue of saturation.

(3) Circular polarization produces dramatically dif-

ferent ATI spectra, at least in part due to the centrifugal barrier experienced by the high-angular-momentum final states.

(4) Finally, ATI itself is still poorly understood. The observation of many processes of different order occurring with the same rate over a large intensity range suggests that we must look beyond perturbation theory for an explanation. There have been theoretical attempts to do this going back at least to Keldysh,<sup>27</sup> but specific predictions have been few and experiments have been slow to provide unambiguous tests of these theories. The success

of predicting the behavior of free electrons may provide a clue to the nature of atomic interactions in intense fields as well.

#### ACKNOWLEDGMENTS

We would like to thank L. DiMauro, J. Custer, and D. Schumacher for consultation and participation in various aspects of the experiments described in this paper. One of us (T.J.M.) wishes to acknowledge support of National Science Foundation (NSF) Grant No. CPE-8417933.

\*On leave from the Institute for Physical Science and Technology, University of Maryland, College Park, MD 20742.

†Permanent address: Physics Department, Columbia University, New York, NY 10027.

<sup>1</sup>P. Agostini, F. Fabre, G. Mainfray, G. Petite, and N. Rahman, *Phys. Rev. Lett.* **42**, 1127 (1979); P. Kruit, J. Kimman, and M. van der Wiel, *J. Phys. B* **14**, L597 (1981); G. Petite, F. Fabre, P. Agostini, M. Crance, and M. Aymar, *Phys. Rev. A* **29**, 2677 (1984).

<sup>2</sup>U. Johann, T. S. Luk, H. Egger, and C. K. Rhodes, *Phys. Rev. A* **34**, 1084 (1986).

<sup>3</sup>M. Crance, *J. Phys. B* **42**, 776 (1979); B. W. Boreham and H. Hora, *Phys. Rev. Lett.* **42**, 776 (1979).

<sup>4</sup>F. Fabre, G. Petite, P. Agostini, and M. Clement, *J. Phys. B* **15**, 1353 (1982).

<sup>5</sup>P. Kruit, J. Kimman, and M. van der Wiel, *J. Phys. B* **14**, L597 (1981).

<sup>6</sup>P. Kruit, J. Kimman, H. G. Muller, and M. J. van der Wiel, *Phys. Rev. A* **28**, 248 (1983).

<sup>7</sup>L. S. Lompre, A. L'Huillier, G. Mainfray, and C. Manus, *J. Opt. Soc. Am. B* **2**, 1906 (1985).

<sup>8</sup>L. A. Lompre, G. Mainfray, C. Manus, and J. Thebault, *Phys. Rev. A* **15**, 1604 (1977).

<sup>9</sup>L. A. Lompre, A. L'Huillier, G. Mainfray, and J. Y. Fan, *J. Phys. B* **17**, L817 (1984).

<sup>10</sup>A. L'Huillier, L. A. Lompre, G. Mainfray, and C. Manus, *Phys. Rev. Lett.* **48**, 1814 (1982); *J. Phys. B* **16**, 1363 (1983); **27**, 253 (1983); T. S. Luk, U. Johann, H. Egger, H. Pummer, and C. K. Rhodes, *Phys. Rev. A* **32**, 214 (1985); P. Agostini and G. Petite, *J. Phys. B* **17**, L811 (1984); D. Sh. Akramova, D. T. Alimov, V. K. Medvedeva, M. A. Prebrazhenskii, M. A. Tursunov, and P. K. Khalibullaev, *Opt. Spektrosk.* **56**, 987 (1984) [*Opt. Spectrosc. (USSR)* **56**, 606 (1984)]; K. X. He, F. Yergeau, and S. L. Chin, *J. Phys. B* **18**, 2615 (1985).

<sup>11</sup>F. Fabre, P. Agostini, G. Petite, and M. Clements, *J. Phys. B* **14**, L677 (1981); R. Hippler, H. Humpert, H. Schwier, S. Jetzke, and H. O. Lutz, *ibid.* **16**, L713 (1983); H. Humpert, H. Schwier, R. Hippler, and H. O. Lutz, *Phys. Rev. A* **32**, 3787 (1985).

<sup>12</sup>M. J. Hollis, *Opt. Commun.* **25**, 395 (1978); B. W. Boreham and H. Gora, *Phys. Rev. Lett.* **42**, 776 (1979); B. W. Boreham

and J. L. Hughes, *Zh. Eksp. Teor. Fiz.* **80**, 496 (1981) [*Sov. Phys.—JETP* **53**, 252 (1981)].

<sup>13</sup>M. Bashkansky, P. H. Bucksbaum, R. R. Freeman, and T. J. McIlrath, in *Short Wavelength Coherent Radiation: Generation and Applications*, edited by D. T. Attwood and J. Bokor (AIP, New York, 1986), p. 174; R. R. Freeman, T. J. McIlrath, P. H. Bucksbaum, and M. Bashkansky, *J. Opt. Soc. Am.* (to be published).

<sup>14</sup>T. W. B. Kibble, *Phys. Rev.* **150**, 1060 (1966); *Phys. Rev. Lett.* **16**, 1054 (1966); H. Hora, *Phys. Fluids* **12**, 182 (1969); *Physics of Laser Driven Plasmas* (Wiley, New York, 1981).

<sup>15</sup>H. G. Muller, A. Tip, and M. J. van der Wiel, *J. Phys. B* **16**, L679 (1983); M. H. Mittelman, *Phys. Rev. A* **29**, 2245 (1984); A. Szoke, *J. Phys. B* **18**, L427 (1985).

<sup>16</sup>P. L. Kapitza and P. A. M. Dirac, *Proc. Cambridge Philos. Soc.* **29**, 297 (1933); W. Kelvin, Cambridge Dublin Math. J., Nov. 1845; also W. Kelvin, *Electrostatics and Magnetism* (1872), p. 21; for a review of the early history see V. I. Pavlov, *Usp. Fiz. Nauk* **124**, 345 (1978) [*Sov. Phys.—Usp.* **21**, 171 (1978)].

<sup>17</sup>J. H. Eberly, *Progress in Optics VII*, edited by E. Wolf (North-Holland, Amsterdam, 1969), p. 361 and references therein; P. Avan, C. Cohen-Tannoudji, J. Dupont-Roc, and C. Fabre, *J. Phys. (Paris)* **37**, 993 (1976); R. J. Cook, D. G. Shankland, and A. L. Wells, *Phys. Rev. A* **31**, 564 (1985).

<sup>18</sup>L. Pan, L. Armstrong, Jr., and J. H. Eberly, *J. Opt. Soc. Am. B* **3**, 1319 (1986).

<sup>19</sup>P. J. Leonard, *At. Data Nucl. Data Tables* **14**, 21 (1974).

<sup>20</sup>T. W. B. Kibble, *Phys. Rev.* **150**, 1060 (1966).

<sup>21</sup>M. J. Hollis, *Opt. Commun.* **25**, 395 (1978).

<sup>22</sup>E. Fiordilino and M. H. Mittleman, *J. Phys. B* **18**, 4425 (1985).

<sup>23</sup>P. H. Bucksbaum, M. Bashkansky, and T. J. McIlrath, *Phys. Rev. Lett.* **58**, 349 (1987).

<sup>24</sup>P. H. Bucksbaum, M. Bashkansky, R. R. Freeman, and T. J. McIlrath, *Phys. Rev. Lett.* **56**, 2590 (1986).

<sup>25</sup>H. B. Bebb and A. Gold, *Phys. Rev.* **143**, 1 (1966).

<sup>26</sup>F. Yergeau, G. Petite, and P. Agostini (unpublished).

<sup>27</sup>L. V. Keldysh, *Zh. Eksp. Teor. Fiz.* **47**, 1945 (1964) [*Sov. Phys.—JETP* **20**, 1307 (1965)].